Electronic Supplementary Information

Computational details

All the spin-polarized first-principles calculations in this work were performed by using Vienna ab-initio simulation package (VASP) based on the density functional theory (DFT).[1] The projector augmented wave (PAW) method[2] was adopted to treat the electron and ion interactions, and the exchange-correlation functional was described with the generalized gradient approximation of Perdew-Burke-Ernzerhof (GGA-PBE).[3] The van der Waals interactions was deal with the Grimme's semiempirical DFT-D3 method.[4] The plane wave energy cutoff was set to 450 eV. The convergence thresholds for total energy and residual force were 10^{-5} eV and 0.02 eV/Å, respectively. The (2 × 2) supercell with a vacuum layer of ~18 Å was employed to simulate the Ti_2O_3(012) surface. For such supercell, the first Brillouin zone was sampled with the Monkhorst-Pack k-point grid of 3 × 3 × 1.[5] The solvation correction was carried out with an implicit solvation model as implemented in VASPsol.[6]

In order to obtain the most stable exposed-terminal of Ti_2O_3(012) surfaces, the surface energy (γ) was calculated with the following formula:[7]

$$\gamma = (E_{unrelax} - nE_{bulk})/2A + (E_{relax} - E_{unrelax})/A$$

where, A is the surface aera of one side of the slab; n is the number of Ti_2O_3 units in the slab; E_{bulk} is the total energy of the bulk Ti_2O_3 formula unit; E_{relax} and $E_{unrelax}$ are the total energies of the slabs with and without structural relaxation, respectively.

The Pourbaix diagrams of Ti_2O_3(012) surface was established by plotting the most stable surface state under the relevant pH and potential (U). In our model, it is assumed that the oxidation of water to form OH* and O* on Ti_2O_3(012) surface follows the two steps:[8]

$$H_2O + * \rightarrow OH^* + H^+ + e^- \quad (1)$$

$$OH^* \rightarrow O^* + H^+ + e^- \quad (2)$$

where, * denotes the adsorption site on the catalyst surface. Thus, if using $M(OH)_x(O)_y$ represents a surface (M) with different coverages of OH* and O*, the total reaction process would be expressed as follows:[9]

$$M + (x + y)H_2O \rightarrow M(OH)_x(O)_y + (2y + x)(H^+ + e^-) \quad (3)$$

According to the computational hydrogen electrode (CHE) model,[10,11] the Gibbs free energy change (ΔG) of reaction (3) at a given pH and potential could be calculated by

$\Delta G = E_{M(OH)x(O)y} + (2y + x)/2E_{H2} - E_M - (x + y)E_{H2O} + \Delta E_{ZPE} - T\Delta S - (2y + x)(eU_{RHE} + k_bT \ln 10 \times pH)$

where $E_{M(OH)x(O)y}$, E_M, E_{H2}, and E_{H2O} are the calculated total energies of the surface with adsorbates, the clean surface, and the gas phase H_2 and H_2O molecules, respectively. ΔE_{ZPE} and ΔS are the changes in zero-point energy and entropy, respectively, which could be acquired by computing the vibrational frequency for the adsorption intermediates and from the NIST database[12] for the gas phase molecules (Table S1). Based on the experimental alkaline conditions, the pH and T were set to 13 and 298.15 K, respectively.

Fig. S1 displays the crystal structure of Ti_2O_3 bulk.[13] According to the experimental HRTEM images and XRD results as well as the relevant theoretical works,[14] the (012) surface was selected to construct the Ti_2O_3 slab model. As shown in Fig. S2, there are five possible terminations for the Ti_2O_3(012) surface. By comparing the surface energies (γ) of different configurations, ultimately, the configuration in Fig. S2a with the lowest γ was determined to study the $2e^-$ ORR performance. Fig. S3 exhibits the calculated Ti_2O_3(012) surface slab model with a (2 × 2) supercell, in which the bottom two O-Ti-O layers (circling with blue frame) were fixed to mimic the bulk and the other four O-Ti-O layers were fully relaxed. We have explored the different number of O* and/or OH* adsorption on the Ti_2O_3(012) surface, corresponding to the coverage ranging from 1/8 to 1 ML, and the optimized configurations are shown in Fig. S4.

Experimental Section

Materials: Ti_2O_3 (99.9%), TiO_2 (99.9%), Titanium oxysulfate were purchased from Aladdin Ltd. Potassium hydroxide (KOH), Isopropyl alcohol (IPA), and carbon paper were bought from Beijing Chemical Corporation. Nafion (5 wt.%) were purchased from Sigma-Aldrich Chemical Reagent Co., Ltd. The Fluorine-doped tin oxide (FTO) was acquired from Luoyang Shangzhuo Technology Co. Ltd. (Henan, China). The water used throughout all experiments was purified

through a Millipore system.

Preparation of H_2 plasma treated TiO_{2-x}: Plasma (commercial 13.56 MHz RF source) with power of 600 W and pressure of 20 Pa is used to treat the TiO_2 nanoparticle in H_2 atmosphere (10sccm) with same irradiation time (35min) at room temperature. The degree of oxygen vacancy defects depends on the distance between the sample and the plasma source. Three batches of samples are placed in different positions to form different degrees of defects.

Characterizations: XRD patterns were obtained from a Shimadzu XRD-6100 diffractometer with Cu Kα radiation (40 kV, 30 mA) of wavelength 0.154 nm (Japan). FTIR spectrum was taken on a BRUKER- EQUINOX-55 IR spectrophotometer. SEM images were obtained using a Quanta FEG 250 field-emission SEM. TEM images were obtained from a Zeiss Libra 200FE transmission electron microscope operated at 200 kV. XPS measurements were performed on an ESCALABMK II X-ray photoelectron spectrometer using Mg as the exciting source. The absorbance data of spectrophotometer were acquired on SHIMADZU UV-1800 UV-Vis spectrophotometer. Electron paramagnetic resonance (EPR) spectra were obtained on a Bruker A300 spectrometer at 298 K. In situ Raman measurements were performed using a Horiba-Xplora Plus confocal microscope with 638 nm laser (1−20 mW). In situ spectroelectrochemistry was performed using an electrochemical workstation (CHI760E, CH Instruments), a Pt counter electrode (Alfa Aesar; Pt mesh) and a Hg/HgO reference electrode in ~20 mL of 0.1 M O_2-saturated PBS. In situ ATR-FTIR measurements were taken on a BRUKER-EQUINOX-55 IR spectrophotometer, a diamond-like carbon was coated onto a Si wafer ($5 \times 8 \times 1$ mm^3) to prepare the internal reflection element (IRE). The coated IRE was ultrasonicated for 2 min with 30 wt.%

concentrated H_2SO_4 followed by rinsing with DI water before experiments. A 50 μL of 2 mg mL^{-1} catalyst ink (no Nafion binder) was dropcast on the IRE and dried under air at room temperature. A glassy carbon paper was placed on top of the catalyst layer for good electrical contact. Glassy carbon rod connected to the IRE, Pt gauze, and Ag/AgCl in 3 M KCl were used as the working electrode, counter electrode, and reference electrode, respectively. An FTIR spectrometer with a mercury cadmium telluride (MCT) detector was used for the in-situ ATR-FTIR measurements. 0.1 M PBS were saturated with O_2 for ORR. Gamry Reference 600 potentiostat is employed during recording of the IR spectra.

Electrochemical test for ORR: Electrochemical measurements were performed using an electrochemical workstation (CHI760E, CH Instruments). For rotating ring disk electrode (RRDE) measurements (disk area: 0.2475 cm^2 ； ring area：0.1866 cm^2), a three-electrode system was built with an RRDE (glassy carbon (GC) disk + Pt ring), a Hg/HgO reference electrode, and a graphite rod counter electrode. The RRDE was polished with 1 μm alumina aqueous suspension for 5 min and 0.05 μm alumina aqueous suspension for 5 min and ultra-sonicated in DI water for 30 s. Pt ring was then electrochemically cleaned in the same potential range. The H_2O_2 production activity was assessed by LSV in O_2-saturated 0.1 M PBS at a scan rate of 20 mV s^{-1} and a rotation speed of 1,600 rpm. During the LSV, the Pt ring potential was held at 1.2 V. A gradual degradation of ring current was observed during the continuous RRDE stability test, which was mainly due to the anion poisoning of Pt ring electrode constantly operated at high potential and can be readily recovered by constant current at low potentials to reduce PtO_x.

The H_2O_2 selectivity was calculated using the following relation:

$$H_2O_2\ (\%) = 200 \times I_r / N / (I_d + I_r / N)$$

where I_r is the ring current, I_d is the disk current and N is the collection efficiency (0.325 after calibration). The collection efficiency (N) was determined using the $[Fe(CN)_6]^{3-/4-}$ redox system. The catalyst-deposited RRDE was soaked in N_2-saturated 0.1 M KNO_3 + 10 mM $K_3[Fe(CN)_6]$, and chronoamperometry was performed at −0.3 V (vs. Hg/HgO) while the ring potential was fixed at 0.5 V (vs. Hg/HgO) for 50 s. The background response was also obtained similarly, but the applied disk potential was 0.5 V (vs. Hg/HgO). The collection efficiency could be calculated as follows:

$$N = (|i_r - i_{r,bg}|) / i_d$$

where $i_{r, bg}$ stands for the background ring current. The result yields that the collection efficiency is 32.5%.

In-situ electrochemical spectroscopy testing: In situ Raman measurements were performed using a Horiba-Xplora Plus confocal microscope with 638 nm laser (1−20 mW) In situ spectroelectrochemistry was performed using an electrochemical workstation (CHI760E, CH Instruments), a Pt counter electrode (Alfa Aesar; Pt mesh) and a Hg/HgO reference electrode in ~20 mL of 0.1 M O_2-saturated PBS. In situ ATR-FTIR measurements were taken on a BRUKER-EQUINOX-55 IR spectrophotometer, a diamond-like carbon was coated onto a Si wafer (5 × 8 × 1 mm^3) to prepare the internal reflection element (IRE). The coated IRE was ultrasonicated for 2 min with 30 wt.% concentrated H_2SO_4 followed by rinsing with DI water before experiments. A 50 µL of 2 mg mL^{-1} catalyst ink (no Nafion binder) was dropcast on the IRE and dried under air at room temperature. A glassy carbon paper was placed on top of the catalyst layer for good electrical contact. Glassy carbon rod connected to the IRE, Pt gauze, and Ag/AgCl in 3 M KCl were used as the working electrode, counter electrode, and reference electrode, respectively. An

FTIR spectrometer with a mercury cadmium telluride (MCT) detector was used for the in-situ ATR-FTIR measurements. 0.1 M PBS were saturated with O_2 for ORR. Gamry Reference 600 potentiostat is employed during recording of the IR spectra.

The electrogeneration of H_2O_2: For the electrosynthesis of pure H_2O_2 using a two-electrode solid electrolyte cell. Anion exchange membranes (AEM) in the form of GaossUnion-103 and cation exchange membranes (Nafion 117) were employed. The cathode, featuring approximately 0.1 mg cm^{-2} of Ti_2O_3 and RuO_2, was loaded onto a hydrophobic carbon paper gas diffusion electrode (with an electrode area of approximately 1 cm^2). This electrode served as the cathode, while the anode consisted of RuO_2. The cathode side facilitated an oxygen feed rate of 30 sccm, while the anode side was continuously supplied with 1 M aqueous PBS at a flow rate of 42 mL h^{-1}.

To quantify the H_2O_2 produced, the samples was collected at certain time and mixed with same volume of titanium oxysulfate solution (6 g L^{-1}). The H_2O_2 yield was measured by using the indicator of titanium oxysulfate. The generated complex compound solution was detected with UV-vis spectrophotometer at the maximum absorption wavelength λ = 406 nm.

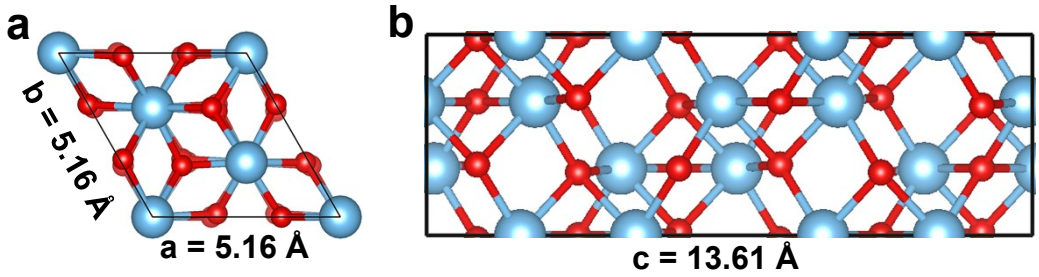

Fig. S1. Top (a) and side (b) views of optimized Ti_2O_3 bulk, together with corresponding lattice constants. The red and light blue balls denote the O and Ti atoms, respectively.

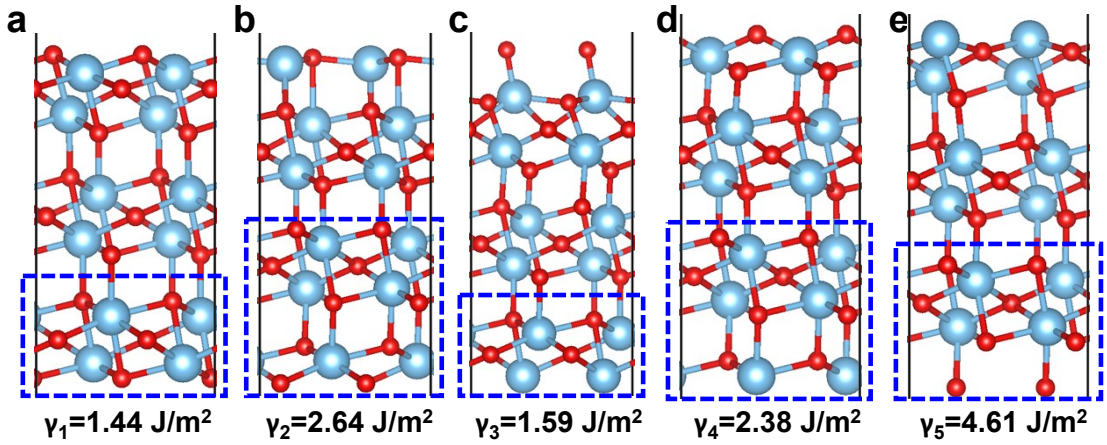

Fig. S2. The possible terminations for $Ti_2O_3(012)$ surface, together with corresponding surface energy (γ). The blue frames circle the fixed atoms. The red and light blue balls denote the O and Ti atoms, respectively.

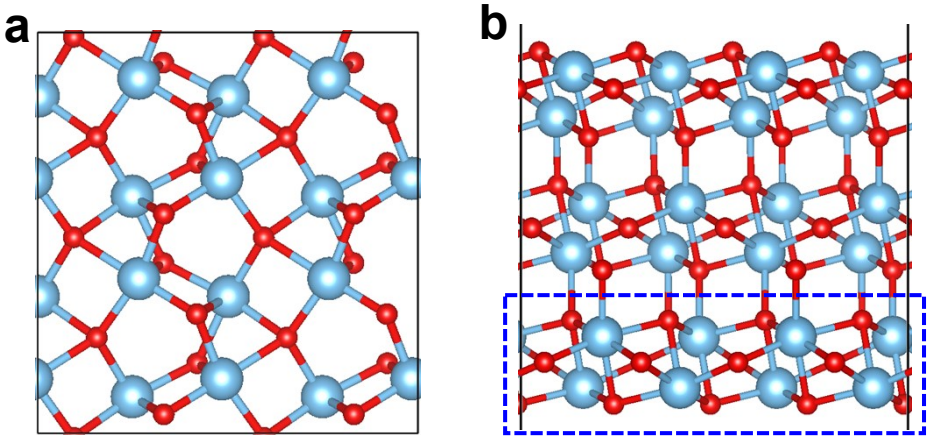

Fig. S3. Top (a) and side (b) views of $Ti_2O_3(012)$ surface slab model with a (2 × 2) supercell. The blue frame circles the fixed atoms. The red and light blue balls denote the O and Ti atoms, respectively.

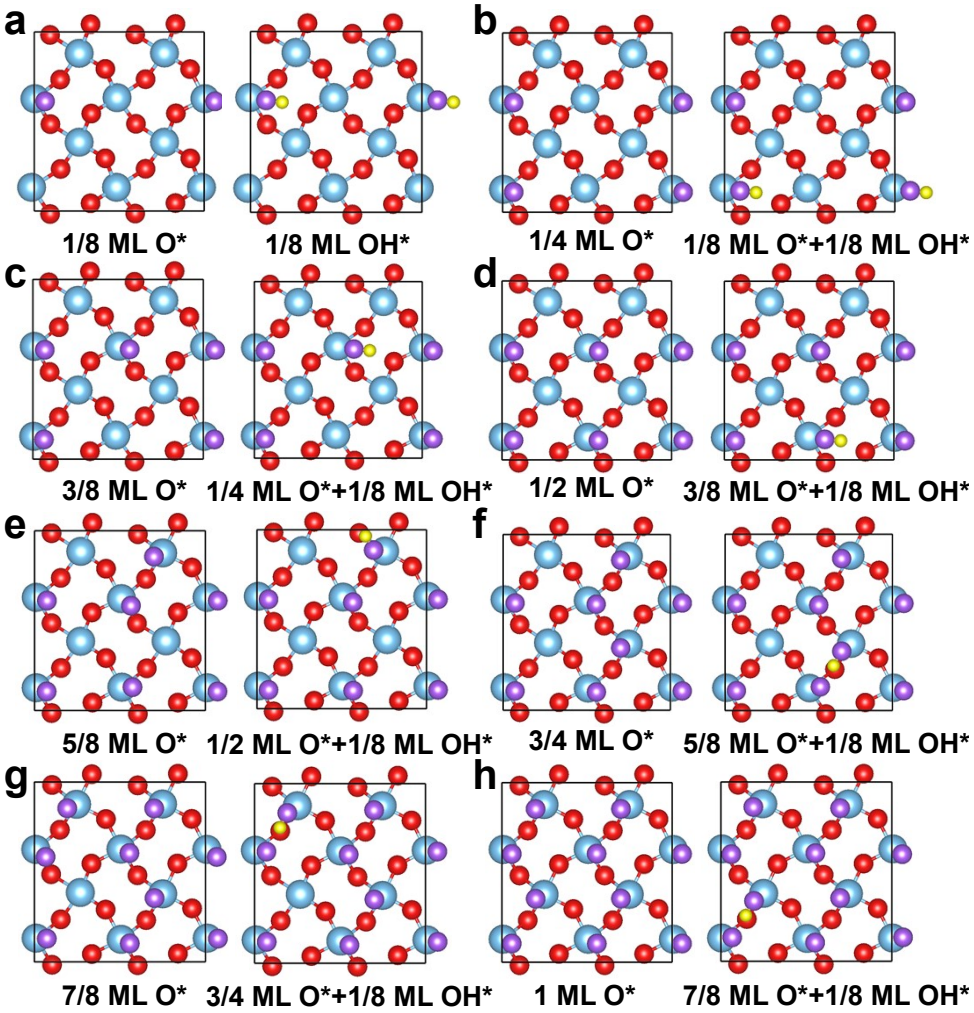

Fig. S4. Atomic models of the most favorable system in thermodynamics for each coverage of O* and/or OH* over Ti_2O_3(012) surface. The stepwise increase of oxygen coverage is shown from a to h. The red and light blue balls denote the O and Ti atoms of the Ti_2O_3(012) surface slab mode, and the purple and yellow balls represent the adsorbed O and H atoms on the surface, respectively.

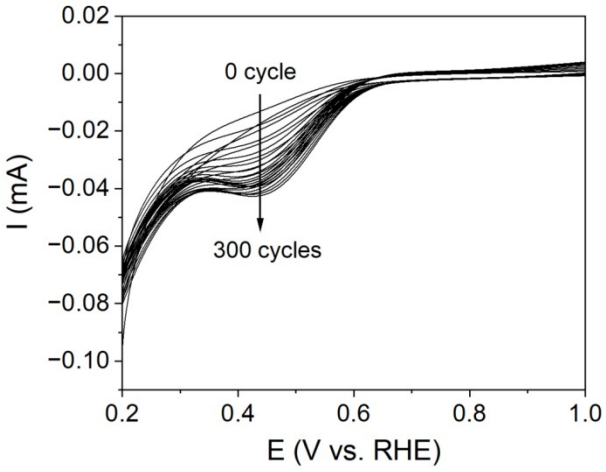

Fig. S5. A comprehensive presentation of CV curves was achieved through a systematic arrangement of these curves in equal intervals, encompassing a total of 300 circles.

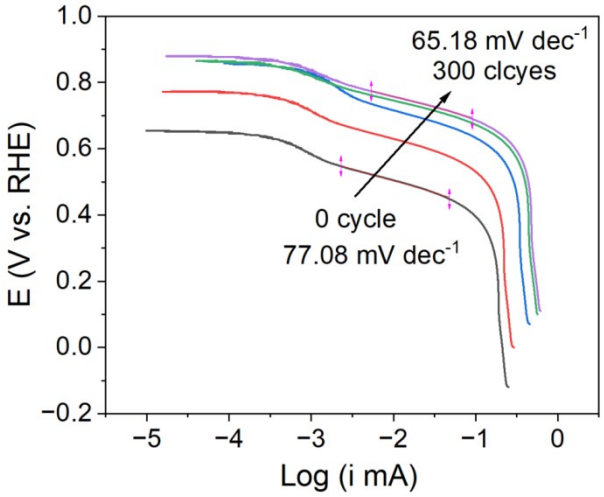

Fig. S6. The Tafel slopes of the LSV curves, extracted from Fig. 2a, encompass the range from cycle 0 to cycle 300. The Fig. clearly illustrates that the progress of the ORR is noticeably influenced by the presence of oxygen-deficient TiO_2 on the surface, resulting in an increasingly accelerated reaction kinetics as the process unfolds.

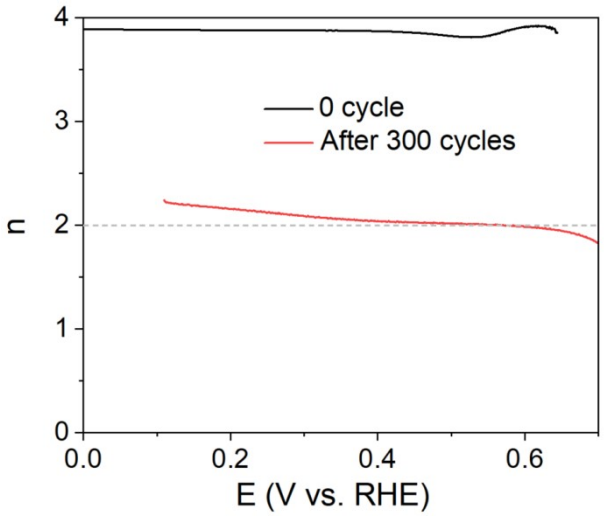

Fig. S7. The quantity of transferred electrons can be determined by examining the LSV curves from the 0th and 300th cycles, as selected from Fig. 2a.

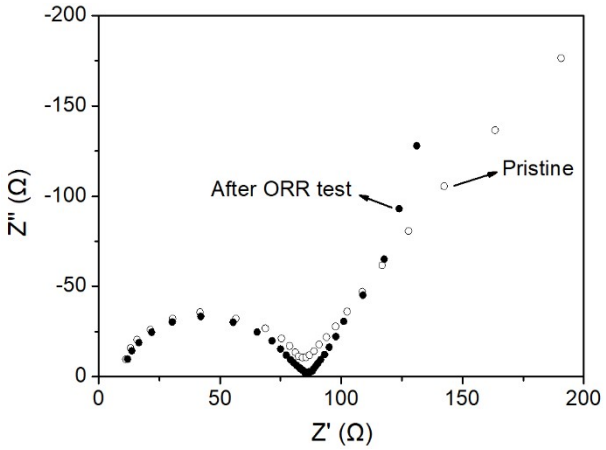

Fig. S8. Impedance spectra before and after the reaction. The initial midnight spectrum reveals that the conductivity following ORR is slightly superior to that of intrinsic Ti_2O_3. This observation suggests that the formation of oxygen-deficient TiO_2 on the surface does not adversely impact the conductivity during the electrocatalytic process.

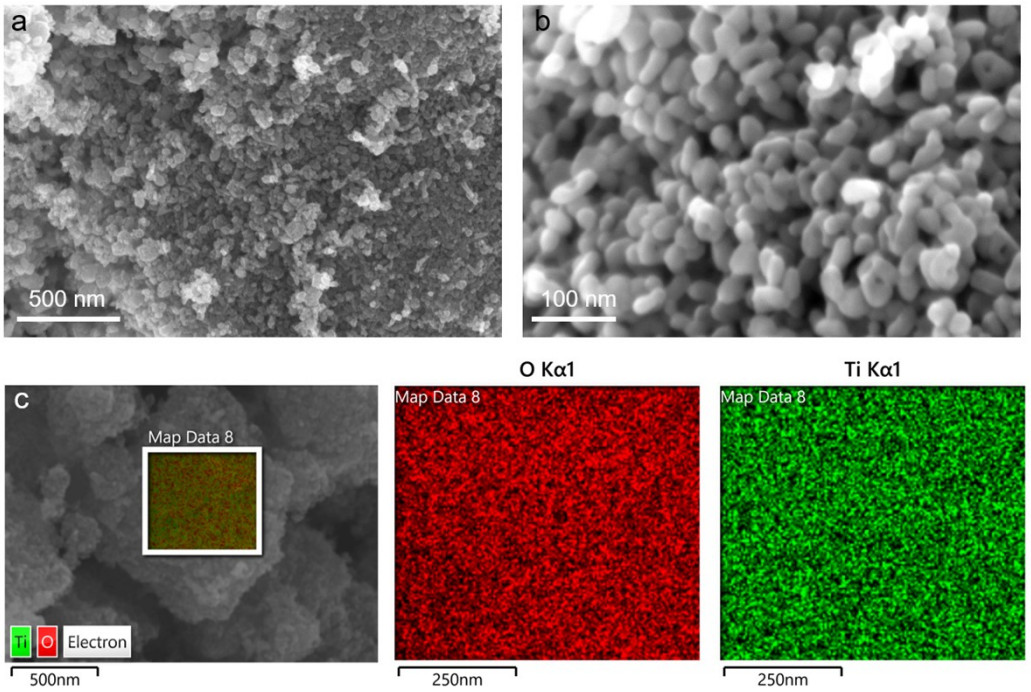

d

Element	Wt.%	Atomic %
O	36.67	62.38
Ti	63.33	37.62
Total:	100.00	100.00

Fig. S9. (a and b) SEM images of Ti_2O_3, along with the corresponding elemental distribution and proportion (c and d), is depicted. The elemental ratio of Ti_2O_3 is found to be in good agreement with the theoretical ratio, indicating a high degree of consistency between the observed and expected elemental proportions.

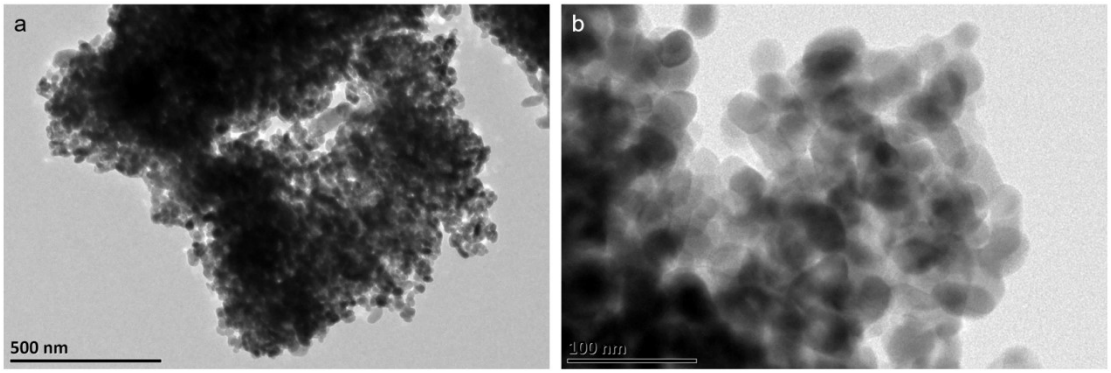

Fig. S10. (a and b) TEM images of Ti_2O_3. The particle size distribution of Ti_2O_3 is predominantly centered around 50nm, exhibiting a spherical morphology.

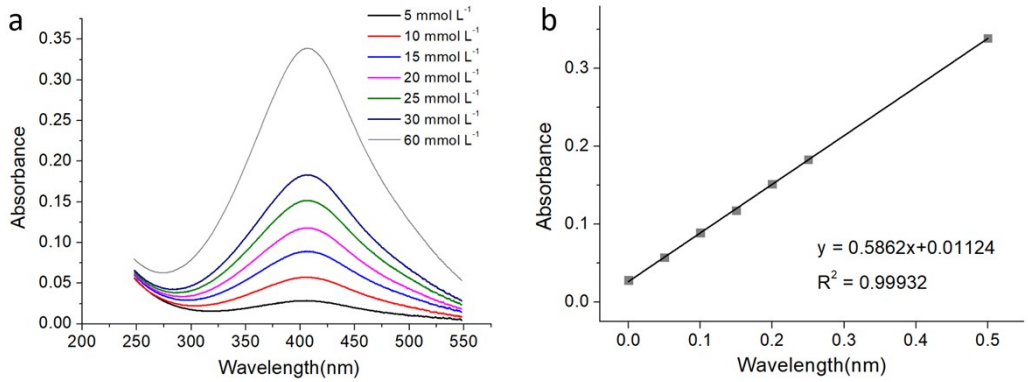

Fig. S11. (a) UV absorption spectra of H_2O_2 solutions with different concentrations, and (b) the corresponding linear fit.

Table S1 The zero-point energy (E_{ZPE}) and the product (TS) of the temperature (298.15 K) and entropy for relevant intermediates and free molecules.

Species	E_{ZPE} (eV)	TS (eV)
O*	0.08	0.07
OH*	0.35	0.09
H_2 (g)	0.27	0.40
H_2O (g)	0.56	0.67

Table S2 Comparing the performance of recently reported electrocatalysts for ORR to H_2O_2.

Electrocatalyst	Electrolyte	Selectivity [%]	Onset potential *vs* RHE	Reference
Reconstructed Ti_2O_3	0.1 M KOH	98.5%	0.78	This work
Bi_2Te_3 NPs	0.1 M KOH	100%	~0.75	15
Co1-NG(O)	0.1 M KOH	82%	0.8V	16
	0.1 M $HClO_4$	/	0.7	16
N-FLG-8	0.1 M KOH	95%	0.8	17
Co–POC–O	0.1 M KOH	84%	0.79	18
MOF NSs-300	0.1 M KOH	99%	0.75	19
Co−N−C	0.1 M KOH	~60%	~0.82	20
	0.5 M H_2SO_4	~80%	~0.78	20
Mo1/OSG-H	0.1 M KOH	95%	0.8	21
O-CNTs	0.1 M KOH	90%	0.8	22
F-mrGO(600)	0.1 M KOH	100%	0.7	23
BN-C1	0.1 M KOH	90%	0.8	24

References

1 R. A. Vargas-Hernández, *Phys. Rev. B*, 1996, **54**, 11169–11186.

2 P. E. Blöchl, *Phys. Rev. B*, 1994, **50**, 17953–17979.

3 J. P. Perdew, J. A. Chevary, S. H. Vosko, K. A. Jackson, M. R. Pederson, D. J. Singh and C. Fiolhais, *Phys. Rev. B*, 1992, **46**, 6671–6687.

4 S. Grimme, J. Antony, S. Ehrlich and H. Krieg, *J. Chem. Phys.*, 2010, **132**, 154104.

5 H. J. Monkhorst and J. D. Pack, *Phys. Rev. B*, 1976, **13**, 5188–5192.

6 K. Mathew, R. Sundararaman, K. Letchworth-Weaver, T. A. Arias and R. G. Hennig, *J. Chem. Phys.*, 2014, **140**, 084106.

7 R. Zhao, Q. Geng, L. Chang, P. Wei, Y. Luo, X. Shi, A. M. Asiri, S. Lu, Z. Wang and X. Sun, *Chem. Commun.*, 2020, **56**, 9328–9331.

8 A. E. Russell, *Phys. Chem. Chem. Phys.*, 2008, **10**, 3722–3730.

9 H. Y. Su, Y. Gorlin, I. C. Man, F. Calle-Vallejo, J. K. Norskov, T. F. Jaramillo and J. Rossmeisl, *Phys. Chem. Chem. Phys.*, 2012, **14**, 14010–14022.

10 G. Gao, A. P. O'Mullane and A. Du, *ACS Catal.*, 2017, **7**, 494–500.

11 J. K. Nørskov, J. Rossmeisl, A. Logadottir, L. Lindqvist, J. R. Kitchin, T. Bligaard and H. Jónsson, *J. Phys. Chem. B*, 2004, **108**, 17886–17892.

12 http:webbook.nist.govchemistry.

13 C. E. Rice and W. R. Robinson, *Acta Crystallogr. Sect. B Struct. Crystallogr. Cryst. Chem.*, 1977, **33**, 1342–1348.

14 M. Gu, Z. Wang, C. Wang and J. Zheng, *Appl. Phys. Lett.*, 2017, **111**, 181603.

15 N. Zhang, F. Zheng, B. Huang, Y. Ji, Q. Shao, Y. Li, X. Xiao and X. Huang, *Adv. Mater.*, 2020, **32**, 1906477.

16 E. Jung, H. Shin, B. H. Lee, V. Efremov, S. Lee, H. S. Lee, J. Kim, W. Hooch Antink, S. Park, K. S. Lee, S. P. Cho, J. S. Yoo, Y. E. Sung and T. Hyeon, *Nat. Mater.*, 2020, **19**, 436–442.

17 C. Tang, L. Chen, H. Li, L. Li, Y. Jiao, Y. Zheng, H. Xu, K. Davey and S. Qiao, *J. Am. Chem. Soc.*, 2021, **143**, 7819–7827.

18 B. Q. Li, C. X. Zhao, J. N. Liu and Q. Zhang, *Adv. Mater.*, 2019, **31**, 1808173.

19 M. Wang, N. Zhang, Y. Feng, Z. Hu, Q. Shao and X. Huang, *Angew. Chem. Int. Ed.* 2020, **59**, 14373–14377.

20 Y. Sun, A. Bagger, N. Ranjbar, W. Ju, J. Li, A. Zitolo, S. Li, L. Silvioli, L. Arnarson, X. Wang, T. Möller, D. Bernsmeier, J. Rossmeisl, F. Jaouen and P. Strasser, *J. Am. Chem. Soc.*, 2019, **141**, 12372–12381.

21 C. Tang, Y. Jiao, B. Shi, J. Liu, Z. Xie, X. Chen, Q. Zhang and S. Qiao, *Angew. Chem. Int. Ed.* 2020, **132**, 9256–9261.

22 Z. Lu, G. Chen, S. Siahrostami, Z. Chen, K. Liu, J. Xie, L. Liao, T. Wu, Di. Lin, Y. Liu, T. F. Jaramillo, J. K. Nørskov and Y. Cui, *Nat. Catal.*, 2018, **1**, 156–162.

23 H. W. Kim, M. B. Ross, N. Kornienko, L. Zhang, J. Guo, P. Yang and B. D. McCloskey, *Nat. Catal.*, 2018, **1**, 282–290.

24 S. Chen, Z. Chen, S. Siahrostami, D. Higgins, D. Nordlund, D. Sokaras, T. R. Kim, Y. Liu, X. Yan, E. Nilsson, R. Sinclair, J. K. Nørskov, T. F. Jaramillo and Z. Bao, *J. Am. Chem. Soc.*, 2018, **140**, 7851–7859.